

Delft University of Technology

Experimental Simulations Post-Test Report

Delft University of Technology, Delft, South Holland, 2628 CD

Bharadwaj Tallapragada	5323622
Changkyu Park	4646061
Malte Wegener	4672194
Martin van Schie	4648366

Submission Date:	March 28, 2021
Course:	AE4115
Group:	23

Contents

1	Introduction	3
2	The experimental setup	4
2.1	Test conditions and approach	5
2.2	Limitations	5
3	Implementation of boundary corrections	6
3.1	Solid blockage	6
3.2	Wake blockage	6
3.3	Lift interference	8
3.4	Downwash correction at tailplane	9
3.5	Slipstream blockage	10
3.6	Implementation of the correction	11
3.7	Impact on the experimental dataset	11
3.8	Limitations	13
4	Analysis of the results	14
4.1	Thrust calculation	14
4.2	Visual analysis	14
4.3	Determination of stability derivatives	15
4.4	Stability of the aircraft	17
4.5	Acoustic Analysis	18
4.6	Limitations	22
5	Conclusion and recommendations	23
	Appendix A Test Matrix	25

Nomenclature

AR	=	Aspect ratio
B	=	Tunnel breadth
b	=	Span
b_e	=	Effective vortex span
b_v	=	Vortex span
C	=	Tunnel cross-sectional area
C_D	=	Drag coefficient
C_{Di}	=	Induced drag coefficient
C_{D0}	=	Drag coefficient at zero lift
C_L	=	Lift coefficient
C'_L	=	Rolling moment coefficient
C_M	=	Pitching moment coefficient
C_N	=	Yawing moment coefficient
C_T	=	Thrust coefficient
c	=	Chord length
d	=	Diameter
f	=	Frequency
H	=	Tunnel height
J	=	Advance ratio
K_1	=	Body shape factor of wing/tailplane
K_3	=	Body shape factor of streamline body of revolution
l	=	Length
N	=	Number of propeller blades
N_{dp}	=	Number of datapoints
q	=	Dynamic pressure
Re	=	Reynolds number
S	=	Model reference area
S_P	=	Propeller disk area
T	=	Thrust
t	=	Maximum thickness
V	=	Velocity
v	=	Volume
α	=	Angle of attack
α_g	=	Geometric angle of attack
β	=	Side slip angle
$\Delta\alpha_{sc}$	=	Upwash at $0.75c$
$\Delta\alpha_{uw}$	=	Upwash at wing at quarter-chord
δ	=	Deflection angle
δ_b	=	Boundary correction factor
δ_r	=	Rudder deflection angle
ϵ	=	Correction factor
τ_1	=	Tunnel-model factor
τ_2	=	Downwash correction factor

Subscripts:

cor	=	Corrected
f	=	Fuselage
ht	=	Horizontal tailplane
n	=	Nacelle
p	=	Propeller
r	=	Rudder
$sb, 1$	=	Solid blockage of wing/tailplane
$sb, 2$	=	Solid blockage of streamline body of revolution
ss	=	Slipstream
T	=	Total
t	=	Tailplane
unc	=	Uncorrected
vt	=	Vertical tailplane
w	=	Wing
wb	=	Wall blockage
∞	=	Freestream/ambient

Abbreviations:

BPF	=	Blade passing frequency
CCW	=	Counter-clockwise
cg	=	Centre of gravity
CW	=	Clockwise
OEI	=	One engine inoperative
OSPL	=	Overall sound pressure level
RMS	=	Root-mean-square
RPS	=	Revolutions per second
SPL	=	Sound pressure level

1. Introduction

As engine technology has improved over the years, engines have become increasingly reliable. Nevertheless, engine failures do occur and as engines are not positioned along the centerline in most aircraft, this has implications on the stability and controllability of the aircraft. As such, it is important to investigate the directional stability and controllability of the aircraft that are discussed in this report in case of an engine failure. The investigation was done in terms of directional stability, rudder effectiveness, control power and trimming in yaw.

The non-dimensional directional stability can be expressed as C_{N_β} whereby subscript N denotes the moment around the z-axis as shown in Figure 1. Subscript β denotes the sideslip angle and its positive direction is defined in Figure 2. For the aircraft to be stable, C_{N_β} has to be negative. The aircraft component that mainly ensures this stability is the vertical tailplane. In one engine inoperative (OEI) condition, the vertical tailplane prevents the aircraft from yaw instability.

The rudder gives the aircraft directional control and its angle is also defined in Figure 2. It is used to point the nose back to the direction of flight in an OEI condition. Therefore, it has to generate sufficient force, under various sideslip angles to counteract the yawing motion to put the aircraft back in stability.

Once the aircraft with an inoperative engine is in stable flight, it has to remain stable and is kept stable by the balance of moments from the rudder and the operative engine. It is thus desired to measure the yaw moment, the corresponding deflection and engine thrust. Thus, not only the rudder angle is varied but also the engine thrust, which is controlled via advance ratio J which is defined as

$$J = \frac{V_\infty}{RPS \cdot d_p}.$$

Ultimately, the main derivatives of interest are those related to the yaw and roll moment due to sideslip, rudder deflection as well as engine thrust. Furthermore, the changes in the derivatives with respect to various angles of attack and Reynolds number Re are to be evaluated. Ultimately, the directional stability and controllability of the aircraft can be captured in the following dimensionless stability derivatives:

$$\begin{aligned} &C_{N_\beta}(Re, \alpha), \\ &C_{N_{\delta_r}}(Re, \alpha), \\ &C_{N_{C_T}}(Re, \alpha), \\ &C_{L'_\beta}(Re, \alpha) \text{ and} \\ &C_{L'_{\delta_r}}(Re, \alpha) \end{aligned}$$

whereby each derivative is denoted as, for example, $C_{N_\beta} = \partial C_N / \partial \beta$.

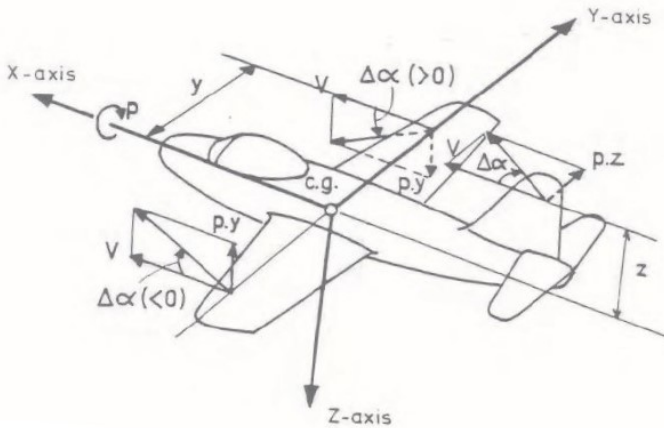


Fig. 1 General coordinate system of aircraft [1]

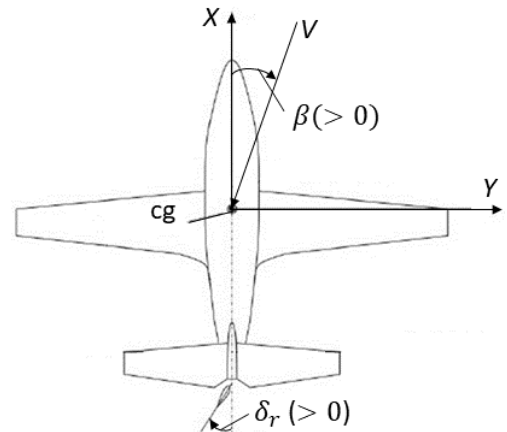


Fig. 2 β and δ_r from top view [1]

2. The experimental setup

The experiment took place in the Low-Turbulence Tunnel (LTT) which is located in TU Delft. This tunnel has an octagonal test section, with a width and height of 1.8 m and 1.25 m respectively. The tunnel is capable of speeds up to 120 m/s, and in typical measurement velocities below 100 m/s, the turbulence level is below 0.1%.

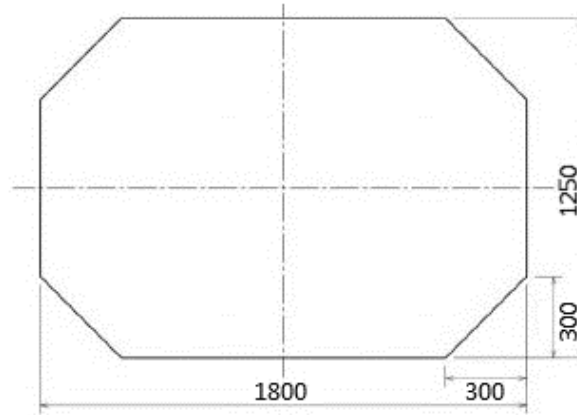


Fig. 3 Octagonal test section of LTT

The model is a conventional tube-and-wing aircraft with an unconventional tail configuration, which implemented the propeller engines into the horizontal stabilizer. Changing the rudder deflection requires the windtunnel to be shut down. The propeller engines could be driven clockwise (CW) and counter-clockwise (CCW). In order to measure the drag of the unpowered aircraft, the propeller blades could be removed and replaced by an aerodynamic nosecone.

The model was upside-down and suspended from an external balance. The model's angle of attack and angle of sideslip could be varied during active windtunnel operations. The balance is able to measure forces and moments for all 6 degrees of freedom. In order to measure the sound emissions of the engine, six near field microphones are mounted on the port side of the fuselage in close proximity to the engine. An isometric view of the tailplane is provided in Figure 4.

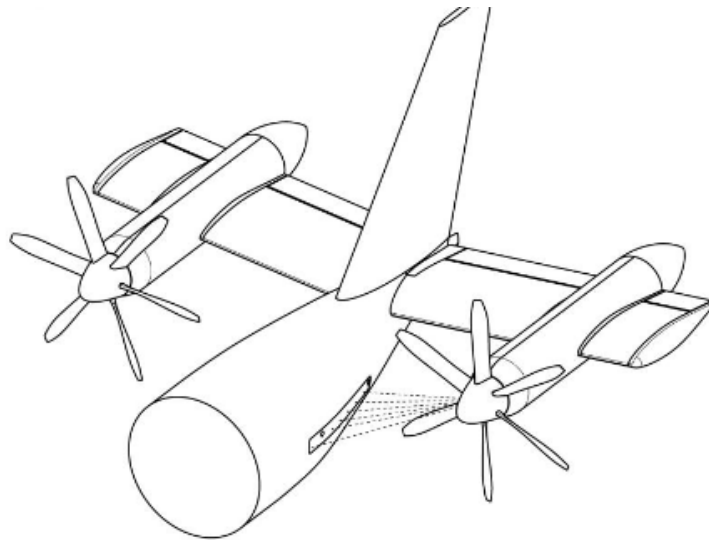


Fig. 4 Isometric view of the tailplane used in the windtunnel model [2]

2.1. Test conditions and approach

The test space is limited by the following operational limitations: V_∞ up to 40 m/s, α between -5 and +14 degrees, β between -10 and +10 degrees, lowest advance ratio of 1.6 at 40 m/s, δ_r between -20 and +20 degrees, and fixed propeller pitch with a choice between CCW, CW and blade-less propellers.

In order to optimally use the given limited windtunnel time, it was decided to vary all parameters only in the linear regime of operations. The lateral symmetry of the aircraft was exploited, by only considering the effect of sideslip for a single direction. To properly evaluate the acoustic effects of the engine, it was chosen to let the starboard engine that is placed away from the microphones be left inoperative. Conditions for sideslip and rudder deflection were chosen, such that they would reflect aircraft operations in sideslipping flight. The ranges selected for all parameters are presented in Table 1. Moreover, the rudder is varied to a maximum deflection of 10 degrees to ensure, that no flow separation will occur at maximum deflection.

Table 1 Available and selected ranges

Variables			Max. Range	Selected range
Rudder angle	δ_r	[deg]	[-20, 20]	[0, -10]
Port engine propeller direction	-	[-]	CW, CCW	CCW
Freestream velocity	V_∞	[m/s]	[0, 40]	[20, 40]
Advance ratio	J	[-]	[1.6, 2.0]	[1.6, 2.0]
Angle of attack	α	[deg]	[-5, 14]	[-3, 7]
Side slip angle	β	[deg]	[-10, 10]	[0, 10]

To maximise the number of different parameter combinations, a response surface design is performed for all parameters, which are able to be varied during active windtunnel operations. As rudder deflection can only be changed when the windtunnel is not running, this parameter was varied independently of the other parameters.

The chosen experimental setup and test approach will allow the calculation of all relevant control derivatives and their change with respect to the angle of attack and Reynolds number in the linear regime. The experiment does not allow for the exact determination of when flow separation will occur. Due to the utilised response surface design approach, the measurement space of interest can be evaluated efficiently in the provided time. The chosen measurement points are shown in Appendix A.

2.2. Limitations

The choices for test points as aforementioned do have their limitations regarding the completeness of information they can provide. Keeping the angles moderate does not allow the investigation of a stall, when it occurs and how severe it could be. However, only the modest operating range of an aircraft is considered and analysed in this report and even in an OEI condition, an aircraft should not be near a stall of any kind. With only the port engine operative, negative β are unlikely as well with reference to positively defined β in Figure 2.

3. Implementation of boundary corrections

Due to the nature of wind tunnel experiments involving surrounding walls that are located close enough to the plane mode, they impose certain undesired effects on the calculated parameters and thus causing the measured parameters to be inaccurate to a small extent. Moreover, the plane model has to be supported by struts to stay off the ground and the effects imposed by these struts are also not part of the wanted results. However, for this experimental analysis, the effect of the struts will not be accounted as they were deemed to have a very minimal influence on the overall analysis of the given measurement challenge. Furthermore, buoyancy effects were neglected as well due to the divergent structure of the test section.

Hence, the measurement data set was corrected for the following: solid blockage, wake blockage, lift interference, downwash correction at tailplane and slipstream blockage for the operative port engine. These will be discussed in the following sections.

3.1. Solid blockage

The solid blockage correction factors were calculated for wing, horizontal tailplane, vertical tailplane, fuselage and nacelles. As given by [3], the correction factors for the wing and the tailplanes could be calculated as

$$\varepsilon_{sb,1} = \frac{K_1 \tau_1 v_{model}}{C^{3/2}} \quad (3.1)$$

while for the fuselage and nacelle, they were calculated as

$$\varepsilon_{sb,2} = \frac{K_3 \tau_1 v_{model}}{C^{3/2}} \quad (3.2)$$

whereby K_1 and K_3 can be retrieved from Figure 5 and τ_1 can be found from Figure 6 using the test section's dimensions.

As the figure does not include the airfoil of the wing of the plane model that was tested, its K_1 value was calculated using equations given by [4] and they are

$$K_1 = \frac{\pi^{3/2} \Lambda}{16(t/c)\kappa_1} \quad (3.3)$$

where

$$\kappa_1 = \frac{v}{bct} \quad (3.4)$$

and

$$\Lambda = \frac{16}{\pi} \int_0^1 \frac{y_t}{c} \sqrt{1-P} \sqrt{1+(dy_t/dx)^2} d\left(\frac{x}{c}\right) \quad (3.5)$$

in which y_t represents the vertical coordinate of base profile at chordwise station x of the airfoil and P is the base profile pressure coefficient at x in an incompressible flow. P was calculated using XFLR5 by loading the provided airfoil coordinates of the wing and creating its base profile version. Ultimately, K_1 of the wing was found to be 1.257. As for the other bodies, the values were able to be taken directly from Figure 5.

3.2. Wake blockage

The wake blockage correction factors are also given by [3] and they are represented as

$$\varepsilon_{wb,T} = \varepsilon_{wb,0} + \varepsilon_{wb,s} \quad (3.6)$$

where

$$\varepsilon_{wb,0} = \frac{S}{4C} C_{D_0} \quad (3.7)$$

and

$$\varepsilon_{wb,s} = \frac{5S}{4C} (C_{D_{unc}} - C_{D_0} - C_{D_i}) \quad (3.8)$$

The values of C_{D_0} and C_{D_i} were found by plotting $C_{L_{unc}}^2$ against C_D and referring to Figure 7. The y-intercept of the plot corresponds to C_{D_0} and the slope of the linear portion corresponds to C_{D_i} . These of course varied with the configuration of the plane model.

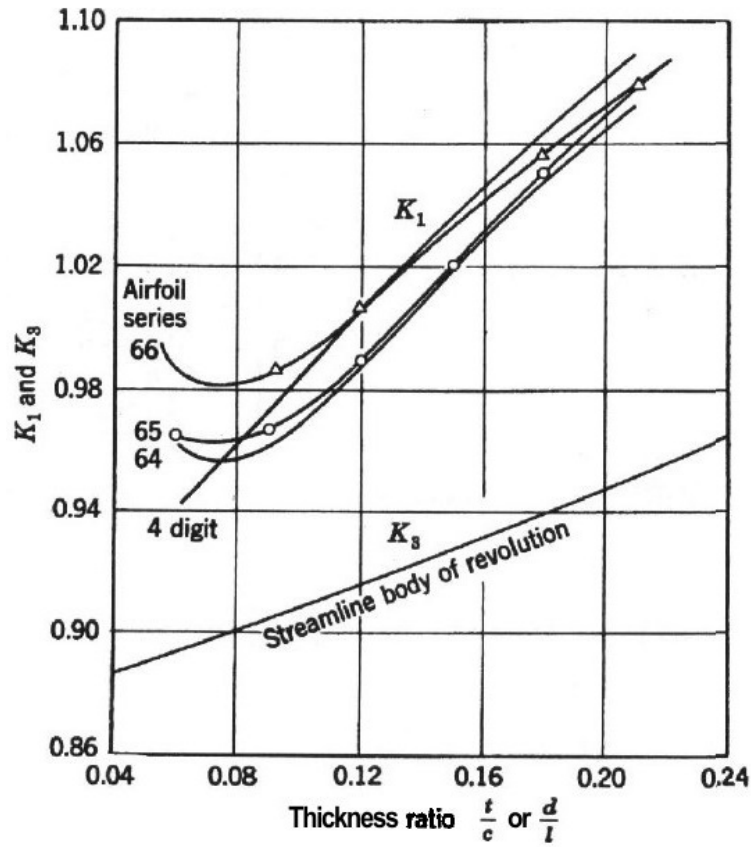


Fig. 5 Values of K_1 and K_3 for bodies [3]

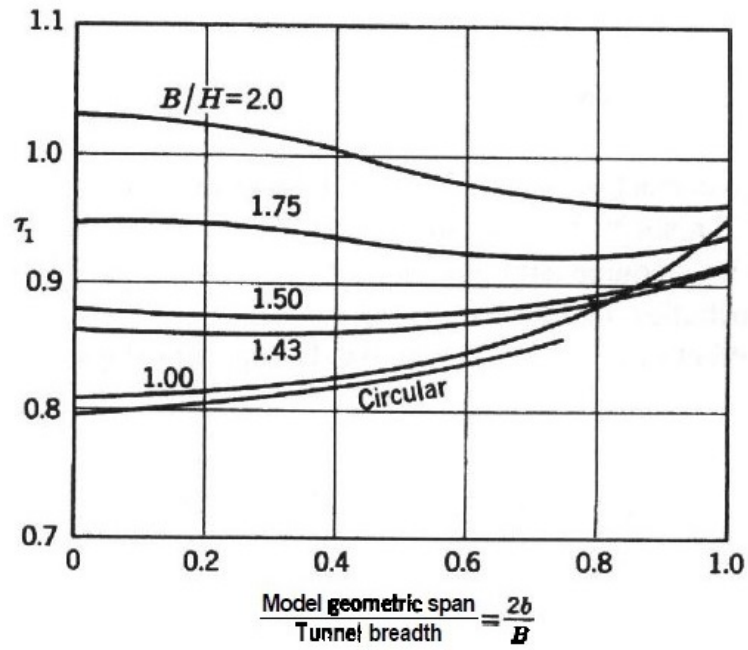


Fig. 6 Values of τ_1 for a number of tunnel types [3]

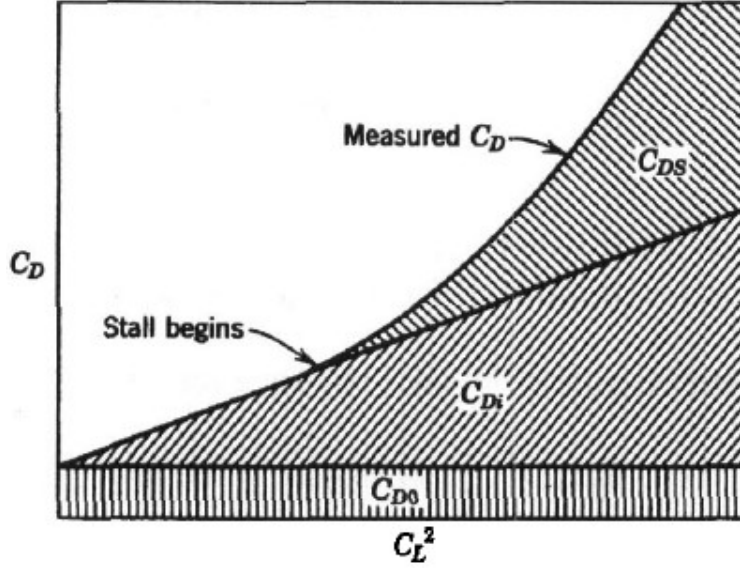


Fig. 7 Drag analysis for a lifting wing [3]

3.3. Lift interference

The upwash and upwash gradient at the wing evaluated at quarter-chord location cause lift interference which has to be accounted for. Since only the wing lift is to be modelled for, the provided tail-off data has been used for the computation. Furthermore, due to the lack of literature of octagonal test sections, data of elliptical test sections were used. The upwash at the wing and the change in drag coefficient are defined as

$$\Delta\alpha_{uw} = \delta \frac{S}{C} C_{L_w} \quad \text{and} \quad (3.9)$$

$$\Delta C_{D_w} = \Delta\alpha_w C_{L_w} \quad (3.10)$$

respectively, where δ can be found using Figure 8 where

$$\begin{aligned} \lambda &= \frac{H}{B}, \\ k &= \frac{b_e}{B} \quad \text{and} \\ b_e &= \frac{b + b_v}{2} \end{aligned}$$

in which b_v is found using Figure 9 and C_{L_w} is retrieved from the tail-off dataset.

There also exists an additional change in angle of attack due to upwash at $0.75c$ which is defined as

$$\Delta\alpha_{sc} = \tau_2(0.5c)\Delta\alpha_w \quad (3.11)$$

whereby $\tau_2(0.5c)$ denotes that it is to be evaluated at half chord meaning the 'tail length' denoted by l_t is ultimately one-quarter of the chord and it can be found from Figure 10. This additional change in angle of attack then induces a pitching moment coefficient which is defined as

$$\Delta C_{M_{0.25c}} = \frac{1}{8} \Delta\alpha_{sc} C_{L_\alpha} \quad (3.12)$$

where C_{L_α} is the slope of linear portion of plot for C_L against α and the total change in angle of attack is

$$\Delta\alpha = \Delta\alpha_{uw} + \Delta\alpha_{sc}. \quad (3.13)$$

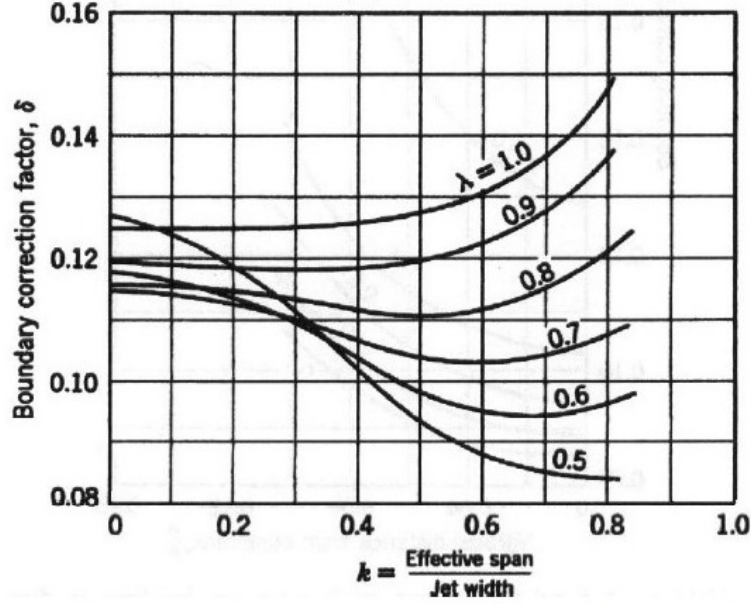


Fig. 8 Values of δ for a wing with uniform loading in a closed elliptic test section [3]

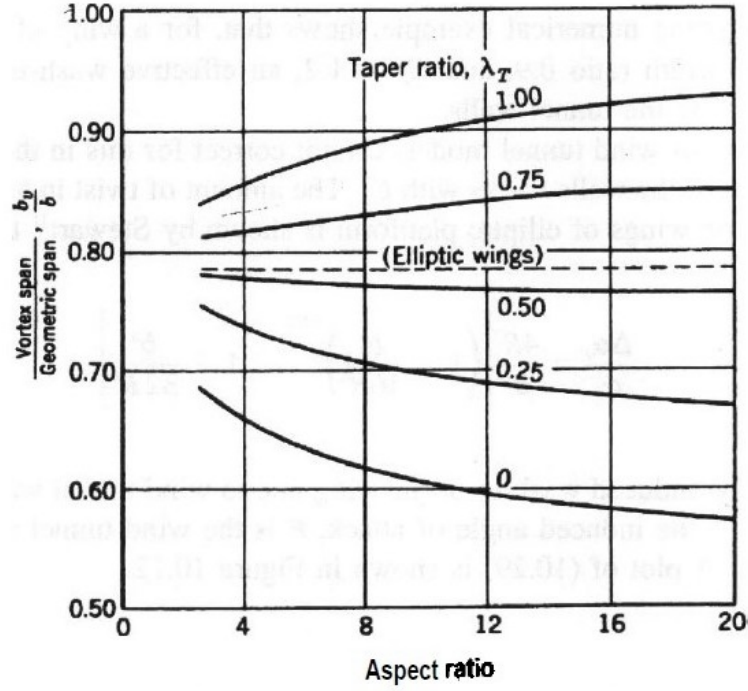


Fig. 9 Values of vortex span for elliptic, rectangular and tapered wings [3]

3.4. Downwash correction at tailplane

The angle of attack at the tailplane also has to be corrected due to the induced velocities from the image vortex system and the effective correction on α_t is

$$\Delta\alpha_t = \Delta\alpha_{uw} + \Delta\alpha_{sc,t} \quad (3.14)$$

where

$$\Delta\alpha_{sc,t} = \delta \frac{S}{C} C_{L_w} \tau_2(l_t) \quad (3.15)$$

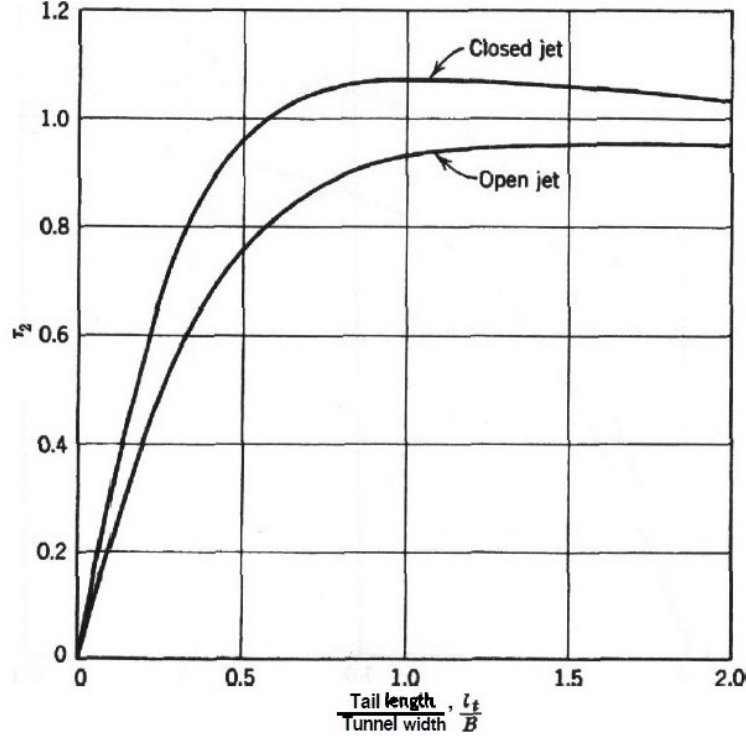


Fig. 10 Values of τ_2 for closed elliptic test section [3]

in which $\tau_2(l_t)$ denotes that the value is evaluated for the distance between the quarter-chord of the wing to the quarter-chord of the tail and it can again be found from Figure 10 and δ from Figure 8. This correction then induces a change in pitching moment coefficient which is represented as

$$(\Delta C_{M_{0.25c}})_t = \left(\frac{\delta C_{M_{0.25c}}}{\delta \alpha_t} \right) \Delta \alpha_t \quad (3.16)$$

whereby $\delta C_{M_{0.25c}} / \delta \alpha_t$ is

$$\frac{\delta C_{M_{0.25c}}}{\delta \alpha_t} = \frac{dC_{L_t}}{d\alpha_t} l_t \quad (3.17)$$

with

$$\frac{dC_{L_t}}{d\alpha_t} = \frac{0.08AR}{AR_t + 2} \frac{q}{q_t} \quad (3.18)$$

as given by [3] and q/q_t was assumed to have a value of 1.

3.5. Slipstream blockage

Due to the propellers on the plane, there is an increased velocity in the slipstream and decreased velocity outside the slipstream. Thus, the measured thrust occurs at a lower velocity in the unbounded domain. As for the given measurement challenge, since one of the two engines is inoperative, the correction was computed accounting for just one propeller. The velocity correction is then

$$V = V_{unc} (1 + \varepsilon_{ss}) \quad (3.19)$$

where

$$\varepsilon_{ss} = -\frac{C_T}{2\sqrt{1 + 2C_T}} \frac{S_P}{C} \quad (3.20)$$

whereby C_T is obtained from the data obtained from measurements.

3.6. Implementation of the correction

Using the various correction factors that were obtained in previous sections, first the freestream velocity and dynamic pressure for blockage are corrected as

$$V = V_{\text{unc}} (1 + \varepsilon) \quad \text{and} \quad (3.21)$$

$$q = q_{\text{unc}} (1 + \varepsilon)^2 \quad (3.22)$$

where

$$\varepsilon = \varepsilon_{\text{sb}} + \varepsilon_{\text{wb}} + \varepsilon_{\text{ss}}. \quad (3.23)$$

Using (3.23), the raw lift and coefficient for blockage were corrected as

$$C_L = C_{L_{\text{unc}}} (1 + \varepsilon)^{-2} \quad \text{and} \quad (3.24)$$

$$C_D = C_{D_{\text{unc}}} (1 + \varepsilon)^{-2} \quad (3.25)$$

and pitching moment correction was neglected as it was not the aim of the given measurement challenge to analyse longitudinal stability. Next, the corrections for lift interference were applied for angle of attack and drag coefficient as

$$\alpha_{\text{cor}} = \alpha_g + \Delta\alpha_{\text{uw}} + \Delta\alpha_{\text{sc}} \quad \text{and} \quad (3.26)$$

$$C_{D_{\text{cor}}} = C_D + \Delta C_{D_w} = C_D + \delta \frac{S}{C} C_{L_w}^2 \quad (3.27)$$

3.7. Impact on the experimental dataset

Using the correction procedure, the plots to compare the dataset before and after correction were produced as shown in Figure 11, Figure 12, Figure 13 and Figure 14 for C_L , C_D , V and α respectively. Firstly for C_L , it can be observed

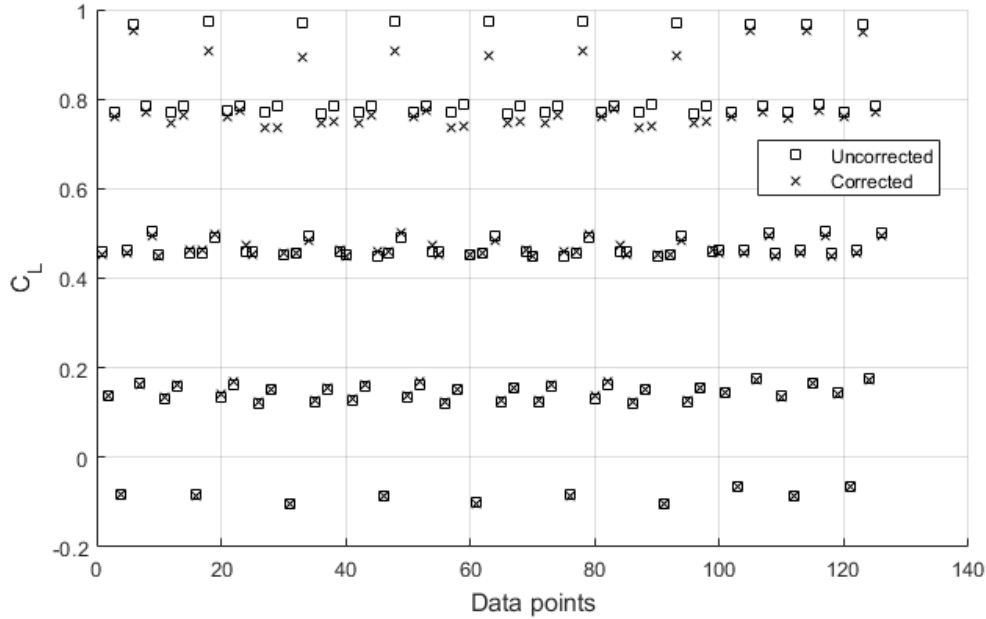


Fig. 11 Comparison between uncorrected and corrected C_L

that for low magnitudes, there is hardly any difference between the uncorrected and corrected dataset. However, with an increase in the magnitude of C_L , the difference increases with corrected C_L being smaller than their uncorrected counterpart for most data points. Similar observation can be made for C_D but there is much more randomness in the dataset with the variation of β , α and δ_r . Moreover, for some groups of the dataset, for example between 25 and 40, the magnitudes of C_D are much lesser than the others but the trend of increasing difference with increasing magnitude still

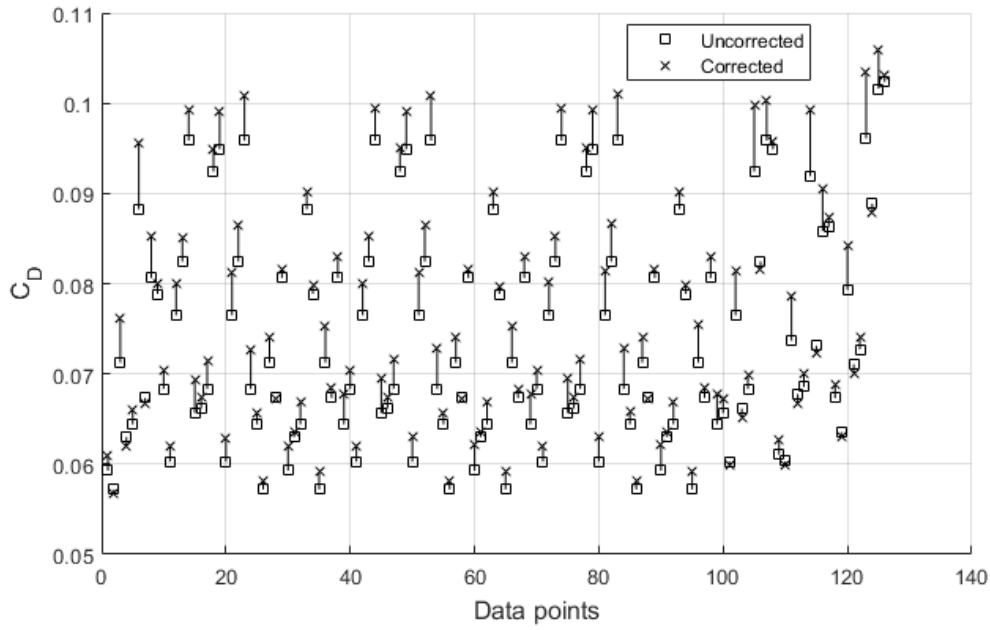


Fig. 12 Comparison between uncorrected and corrected C_D (lines connect the pairs)

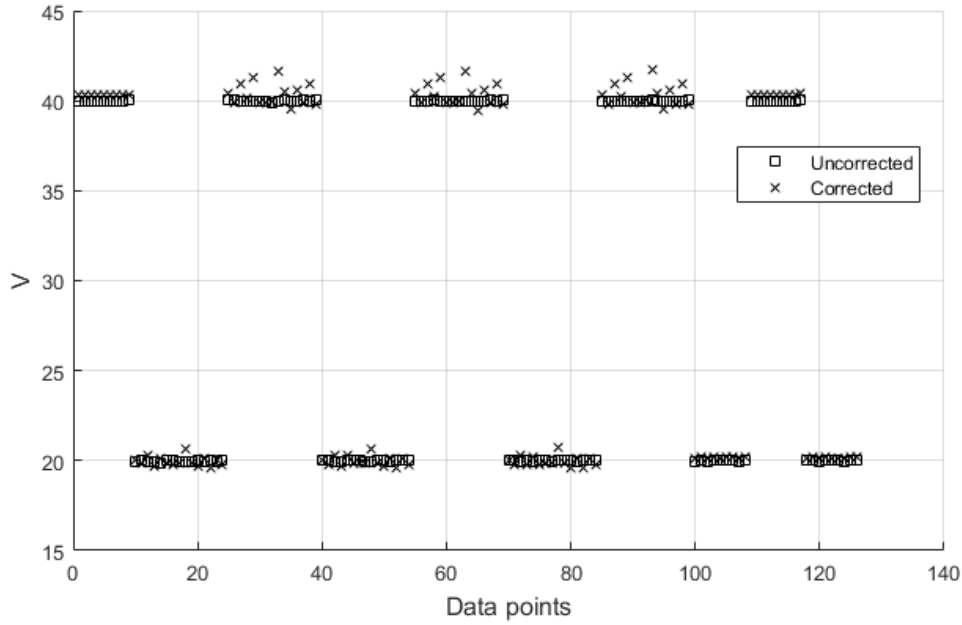


Fig. 13 Comparison between uncorrected and corrected V

stands.

The flow velocities comparison shown in Figure 13 were also not largely affected by the corrections with most groups (polars) of the dataset remaining almost constant. There were, however, slight differences for $V = 40$ m/s for the three middle groups of the dataset. As for α comparison shown in Figure 14, hardly any difference between the uncorrected and corrected datapoints could be observed.

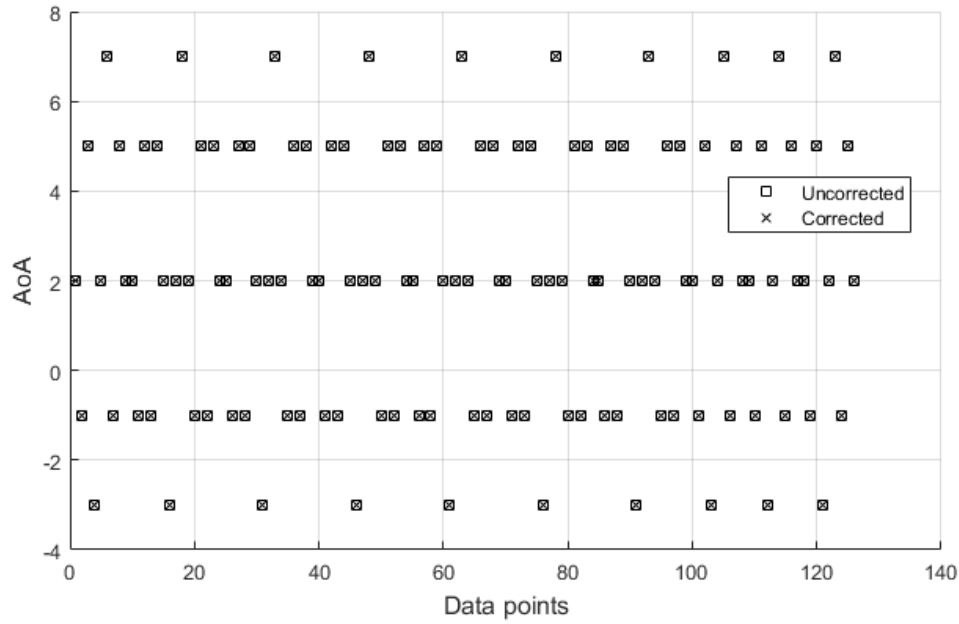


Fig. 14 Comparison between the uncorrected and corrected angle of attack α

In all, it was concluded that the boundary corrections would not have a significant amount of influence on the overall analysis for the directional stability and controllability of the model aircraft.

3.8. Limitations

A few limitations leading to imperfections could be noted. For τ_1 , δ and τ_2 shown in Figure 6, Figure 8 and Figure 10 respectively, the reference data in these plots corresponds to elliptical test sections whereas the actual test section used in the experiment was octagonal. This difference had to be made due to the lack of available literature regarding octagonal test sections, especially one that contains similar dimensions as the one used. Thus, some inaccuracies could have been induced. It is thus recommended to gather as much data as possible for various octagonal test sections and retrieve the values for the one in LTT using interpolation or extrapolation.

With the given measurement challenge conducting analysis for directional stability, correction for sidewash could have improved the accuracy of the analysis. With the sidewash being able to correct for the yaw moment coefficient, checking for the significance of its magnitude would have made the analysis more complete.

Lastly, it is to be noted that the struts were ignored in the blockage corrections due to sheer complexity in accounting for the geometry of the strut structures and also retrieving relevant literature for their non-streamline shape. Although it is assumed that the struts would not impose a significant amount of blockage correction, its implementation would have also contributed to the completeness of the analysis.

4. Analysis of the results

The experiment is performed at $V = 20$ m/s and $V = 40$ m/s, corresponding to Reynolds numbers of $2.3 \cdot 10^5$ and $4.6 \cdot 10^5$ respectively. After calculating the coefficient of thrust, the results are analysed visually to determine if all the recorded values fall into the linear range of response of the aircraft model or if non-linear flow effects such as flow separation take place. With these results in mind, the relevant stability derivatives can be calculated for the linear regime. The stability derivatives can then be used to assess the stability of the aircraft in a one engine inoperative situation.

4.1. Thrust calculation

To calculate the coefficient of thrust, drag measurements of clean configuration were taken. The thrust was calculated as the difference between the drag measurements of a clean configuration and the drag measurements of the powered configuration. The thrust was then non-dimensionalised as

$$C_T = \frac{T}{\rho_{\infty} n^2 D^4}. \quad (4.1)$$

The results were visually verified against the isolated propeller in the reference data of [2] as shown in Figure 15.

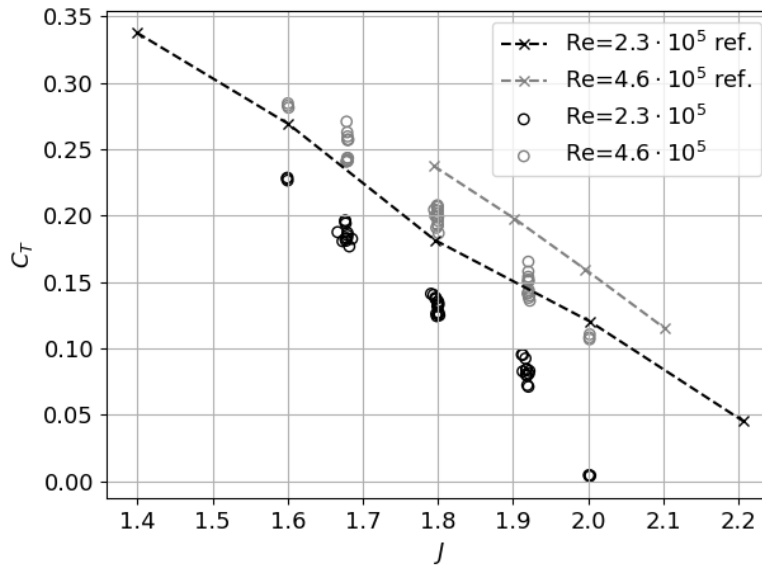
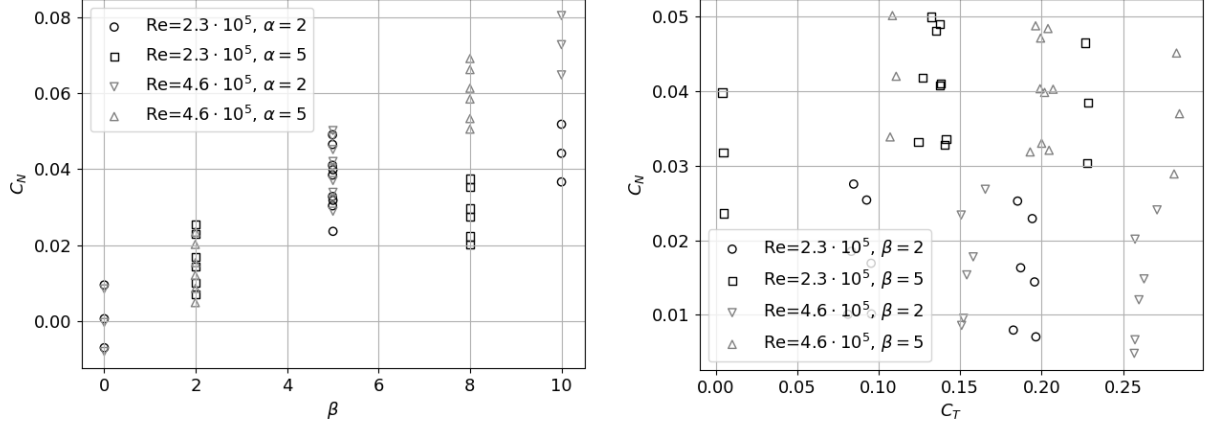


Fig. 15 Coefficient of thrust against advance ratio for experimental data of the integrated propeller and reference data of the isolated propeller

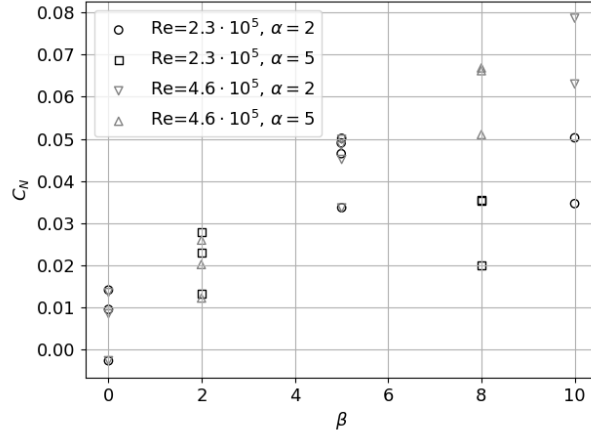
It can be seen that the values for the thrust coefficient are clustered closely for each advance ratio. The value of C_T decreases with increasing advance ratio, which is expected as a higher advance ratio, at constant freestream velocity, indicates a lower rotational speed of the propeller. The slope of the thrust coefficient matches the provided reference data but the magnitude of C_T does not. This is to be expected as the isolated propeller does not interfere with parts of the aircraft thus being able to output higher C_T .

4.2. Visual analysis

In order to identify non-linear flow phenomena and separations, as a first step, C_N is plotted for different angles of sideslip and angles of attack and for varying coefficient of thrust. The resulting figure can be found in Figure 16.



(a) Yaw moment coefficient for different angles of attack and (b) Yaw moment coefficient for different coefficients of thrust angles of sideslip in powered condition



(c) Yaw moment coefficient for different angles of attack and angles of sideslip in unpowered condition

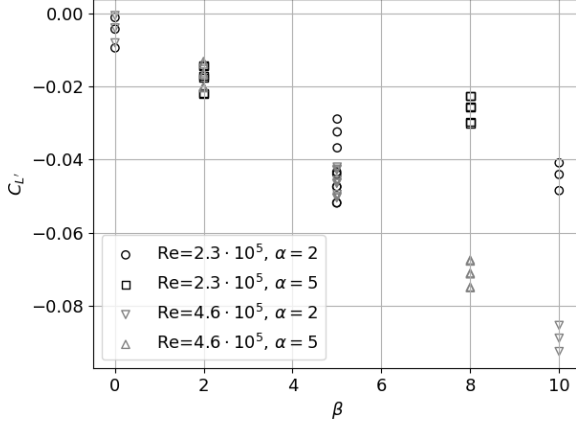
Fig. 16 Scatter plots of yaw moment coefficient for different flight conditions

From the figures, it can be seen that for $\beta > 5$ and small C_T , the values of C_N do not follow the linear trend anymore for $Re = 2.3 \cdot 10^5$. Thus for further analysis and determination of stability derivatives, these datapoints were excluded. The slope in this region is consistent with the slope for smaller angles of attack. As this separated region occurs for every rudder deflection, a systematic error cannot be ruled out. A similar visual inspection is performed for the roll moment coefficient C_L' and it is presented in Figure 17.

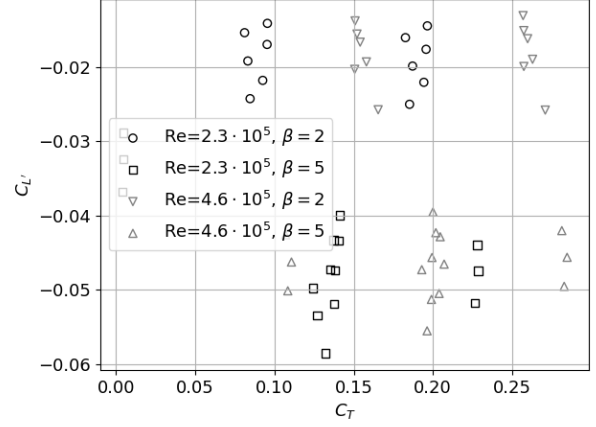
Similar behaviour as previously discussed yaw moment can be observed for the roll moment. For this reason, all datapoints with $\beta > 5$ and very small C_T are not used for stability derivative analysis of the low-speed run. From the visual analysis, the aircraft response can be considered linear under the restrictions mentioned before. Similarly to the previous discussion on yaw moment, a systematic error in the measurement of roll moment cannot be ruled out.

4.3. Determination of stability derivatives

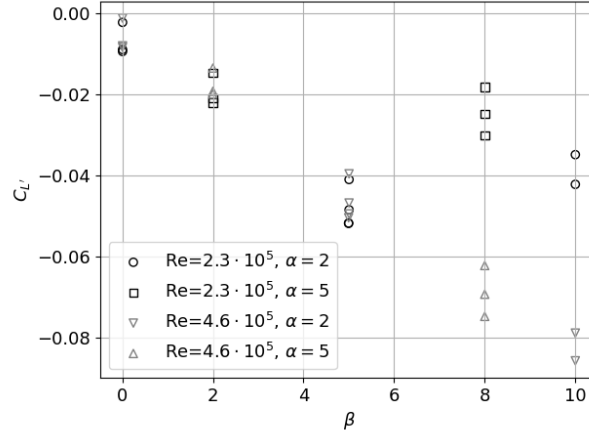
In order to determine the stability derivatives, a linear response of the aircraft is assumed. In order to determine the stability derivatives, multilinear least squares regression is performed on the data. The independent variables are chosen as β , α , δ_r and C_T . The resulting response surfaces are described by



(a) Roll moment coefficient for different angles of attack and angles of sideslip in powered condition



(b) Roll moment coefficient for different coefficients of thrust in powered condition



(c) Roll moment coefficient for different angles of attack and angles of sideslip in unpowered condition

Fig. 17 Scatter plots of roll moment coefficient for different flight conditions

$$C_N = C_{N\beta}\beta + C_{N\alpha}\alpha + C_{N\delta_r}\delta_r + C_{N_{C_T}}C_T + C_1 \quad \text{and} \quad (4.2)$$

$$C'_L = C'_{L\beta}\beta + C'_{L\alpha}\alpha + C'_{L\delta_r}\delta_r + C_2. \quad (4.3)$$

The resulting fit is judged by its R^2 value. The values are recorded and presented together with the number of datapoints used in Table 2 for each of the 4 response surfaces modelled.

Table 2 R^2 values of the performed multilinear regressions

	Re	Powered	R^2	N_{DP}
C_N	$2.3 \cdot 10^5$	X	0.9956	27
C_N	$4.6 \cdot 10^5$	X	0.9956	45
C'_L	$2.3 \cdot 10^5$	X	0.9885	27
C'_L	$4.6 \cdot 10^5$	X	0.9916	45
C_N	$2.3 \cdot 10^5$		0.9860	19
C_N	$4.6 \cdot 10^5$		0.9874	27
C'_L	$2.3 \cdot 10^5$		0.9868	19
C'_L	$4.6 \cdot 10^5$		0.9841	27

From the results, it can be seen that the experimental values do not differ significantly from the fitted surfaces. As for all the surfaces, the number of datapoints significantly exceeds the degrees of freedom of the surface thus overfitting to the data is considered very unlikely. The resulting stability coefficients are presented in Table 3 and Table 4.

Table 3 Yaw stability derivatives

Re	powered		unpowered	
	$2.3 \cdot 10^5$	$4.6 \cdot 10^5$	$2.3 \cdot 10^5$	$4.6 \cdot 10^5$
C_{N_α} [1/rad]	-0.0082	-0.0167	-0.0114	-0.0160
C_{N_β} [1/rad]	0.4523	0.4250	0.4084	0.3876
$C_{N_{\delta_r}}$ [1/rad]	-0.0889	-0.0920	-0.0760	-0.0786
$C_{N_{C_T}}$ [-]	-0.0421	-0.0298	-	-

Table 4 Roll stability derivatives

Re	powered		unpowered	
	$2.3 \cdot 10^5$	$4.6 \cdot 10^5$	$2.3 \cdot 10^5$	$4.6 \cdot 10^5$
$C_{L'_\alpha}$ [1/rad]	0.0437	0.0618	0.0471	0.0560
$C_{L'_\beta}$ [1/rad]	-0.5217	-0.5278	-0.4996	-0.4862
$C_{L'_{\delta_r}}$ [1/rad]	0.0457	0.0444	0.0509	0.0495

From the values, it can be seen that the Reynolds number has an effect of less than 10% for all derivatives except for derivatives with respect to α . In the analysis of roll stability derivatives, the derivative with respect to thrust coefficient was omitted as its magnitude was found to be an order of magnitude lower than the other derivatives. When comparing the aircraft in powered condition to the aircraft in unpowered condition, it was noticed that the yaw moment stability derivatives decrease in magnitude for the unpowered flight, yielding a less stable and less controllable aircraft. On the other hand, the roll moment derivatives do not display a uniform response to a change from powered condition to unpowered condition. $C_{L'_\beta}$ and $C_{L'_\alpha}$ decrease in magnitude in unpowered condition, while $C_{L'_{\delta_r}}$ increase in magnitude.

4.4. Stability of the aircraft

In order for the aircraft to be stable in sideslipping flight, C_{N_β} should be positive [1]. This is the case for this aircraft under analysis. From the derivatives, it can be seen that increasing the engine thrust will increase the sideslip angle, which is expected. It can furthermore be seen that an increase in the angle of attack will result in a higher sideslip angle if all other control inputs are kept constant. By comparing C_{N_β} and $C_{N_{\delta_r}}$, it can be seen that 2.2 degrees of rudder deflection are needed to maintain a single degree of sideslip. In sideslipping flight, a negative $C_{L'_\beta}$ is preferable [1] which is present in the tested aircraft. From these results, it can be concluded, that the aircraft is stable and controllable in OEI condition.

4.5. Acoustic Analysis

The acoustic measurements were performed using the six microphone array placed at the port side rear end of the fuselage along the centreline. The microphones were placed at different directivity angles and are numbered ascending in a streamwise direction. During the performance of the experiment, the sixth microphone malfunctioned and hence, its results were not included in the report. The scaling was performed using the non-dimensional parameters $P_{RMS} d^2/T$, J and f/BPF , where $BPF = RPS \cdot N$. The normalized SPL was calculated using the equation:

$$SPL = 20 \cdot \log_{10} \left(\frac{P_{RMS} d^2}{T} \right) \quad (4.4)$$

The noise generated in the wind tunnel can be split into two categories, namely, tonal and broadband. Tonal noise can be identified by distinct sharp peaks at particular frequencies, whereas the broadband noise is spread continuously over a range of frequencies.

It can be seen in Figure 18 that there are distinct peaks observed at the fundamental blade passing frequencies (BPF). It can also be noticed that as the advance ratio increases, the tonal amplitudes increase causing the tonal peaks to be more distinct as well. The advance ratios of $J = 1.6$ and $J = 2$ correspond to the lowest and highest advance ratios of the dataset. Therefore, it can be assumed that for other advance ratios, a similar trend will be observed as well. Another observation is that tonal peaks can be seen at multiples of $(1/6)$ -th BPF as well. This might be because of the harmonics of the propeller shaft being close to the $(n/6)$ -th BPF.

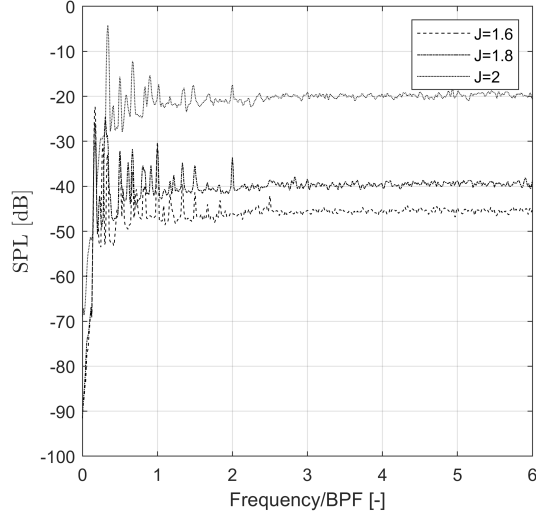
It can be seen from Figure 19 that as the Reynolds number increases, the amplitude of the pressure jump decreases significantly after the first harmonic for the random noise sources. It is also observed that as the scaled frequency increases at a high Reynolds number, the pressure peaks decay more rapidly and the tonal peaks of the propeller are not very noticeable. A possible reason for this could be that the loading on the blade and the tip Mach number were low such that the harmonics of the BPF were not strong enough to be separated from the background noise data.

Furthermore, the effect of rudder deflection at different advance ratios and Reynolds number was analysed as shown in Figure 20 and Figure 21. Data is presented corresponding to microphone 4, as it is located in the plane of rotation of the propeller. It is seen in Figure 20 that at a low Reynolds number, rudder deflection does not induce any significant difference in the tonal noise, irrespective of the advance ratio. Moreover, the trend of increase in tonal noise as advance ratio increases still holds true even at different rudder deflection angles. But, as the Reynolds number increases as seen in Figure 21, it is observed that higher tonal noise is associated with high rudder deflection angles. This phenomenon is significantly more noticeable at high advance ratios as seen in Figure 21b.

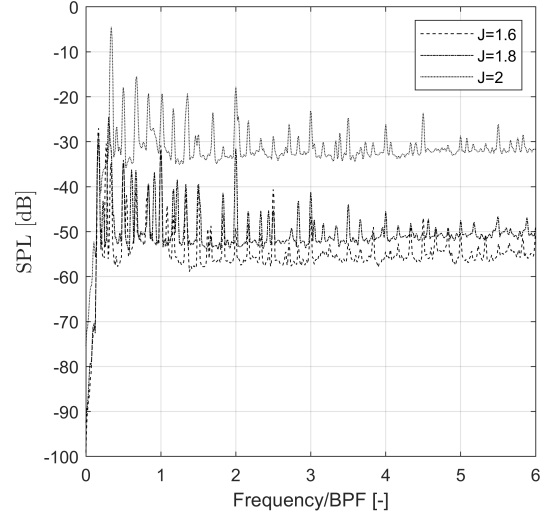
Figure 22 shows the variation in the OSPL at different sideslip angles, at different Reynolds numbers and constant advance ratio. The OSPL is calculated as

$$OSPL = 10 \cdot \log_{10} \left(10^{\sum \frac{SPL_i}{10}} \right). \quad (4.5)$$

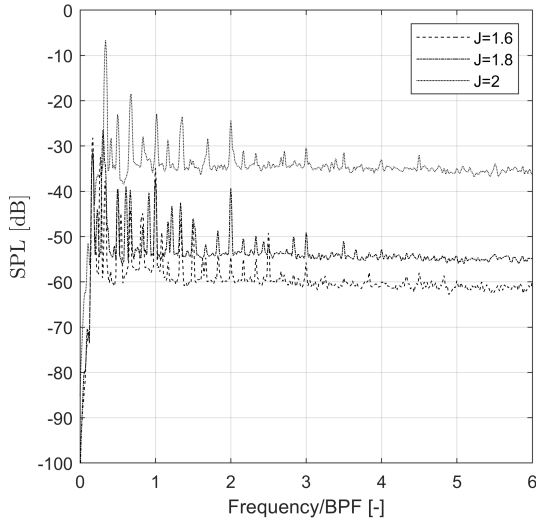
It is observed that at a low Reynolds number, as the sideslip angle increases, the normalized OSPL decreases. But, as the Reynolds number increases, the sideslip angle has a negligible effect on the OSPL values. Another observation that can be drawn from Figure 22 is that as the Reynolds number increases, the OSPL value decreases. It is to be noted that since the six microphones are at different distances along the fuselage, the OSPL values of different microphones cannot be compared as the OSPL is a function of the distance from the source.



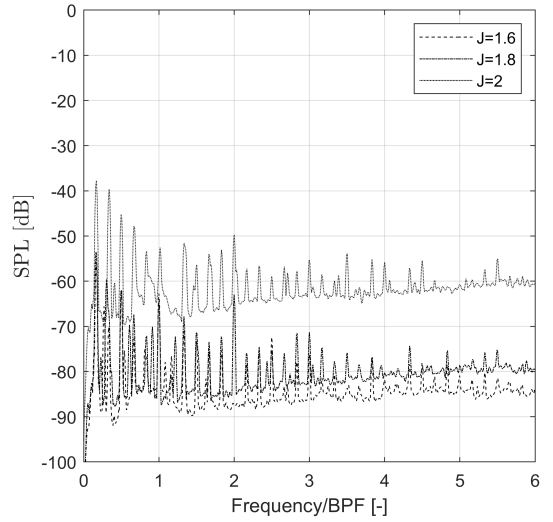
(a) Microphone 1



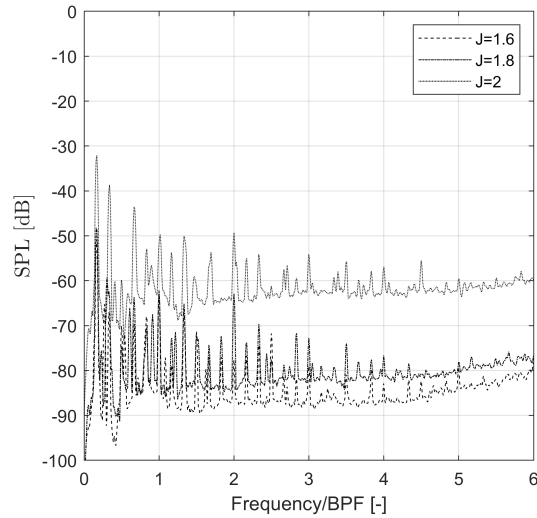
(b) Microphone 2



(c) Microphone 3

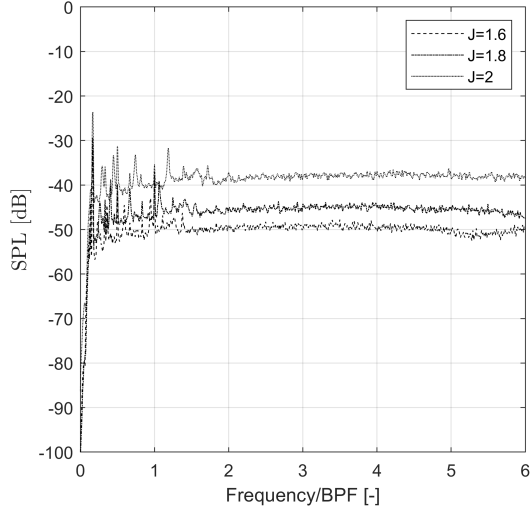


(d) Microphone 4

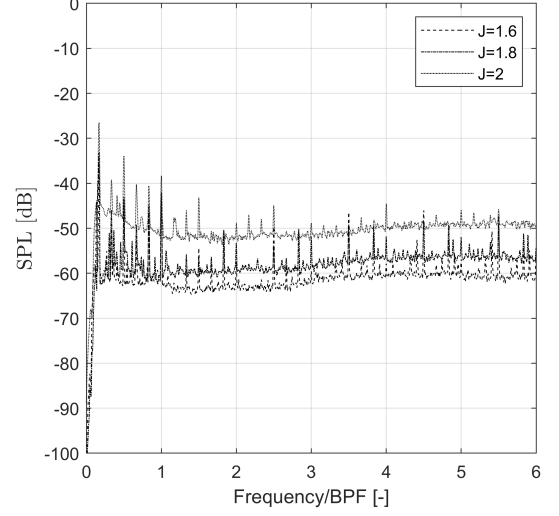


(e) Microphone 5

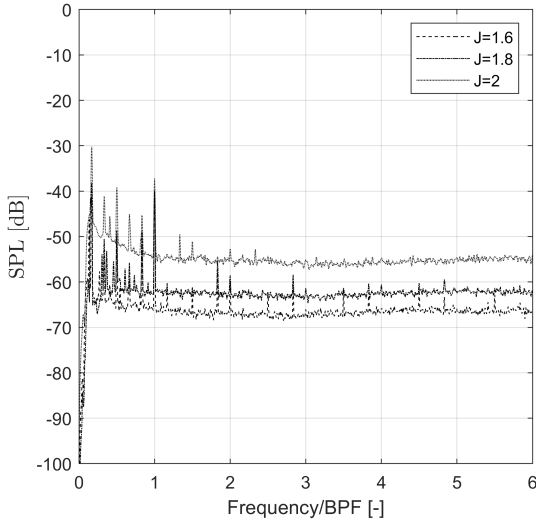
Fig. 18 Normalized SPL vs scaled frequency at $Re = 2.3 \cdot 10^5$, $\alpha = 2$, $\beta = 5$



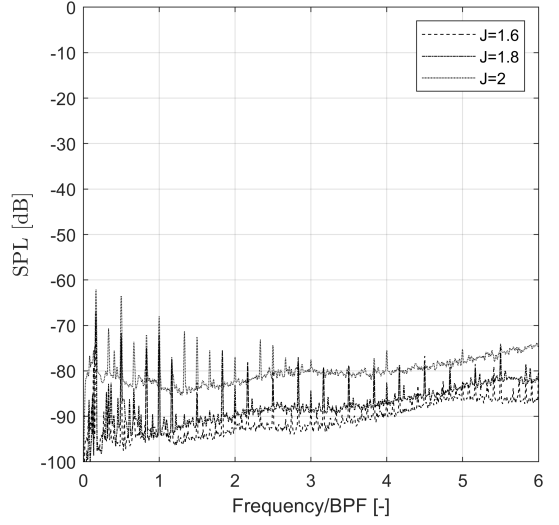
(a) Microphone 1



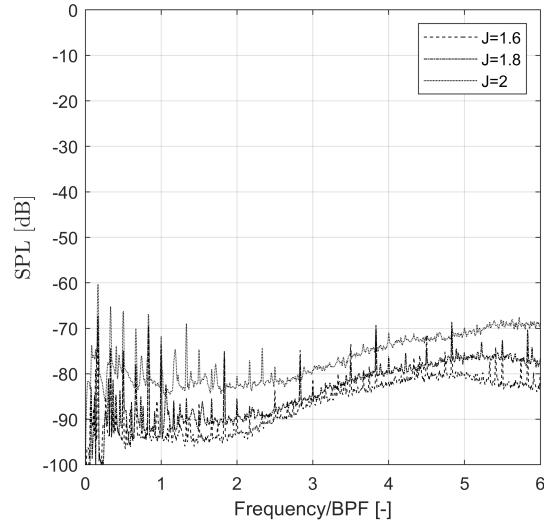
(b) Microphone 2



(c) Microphone 3



(d) Microphone 4



(e) Microphone 5

Fig. 19 Normalized SPL vs scaled frequency at $Re = 4.6 \cdot 10^5$, $\alpha = 2$, $\beta = 5$

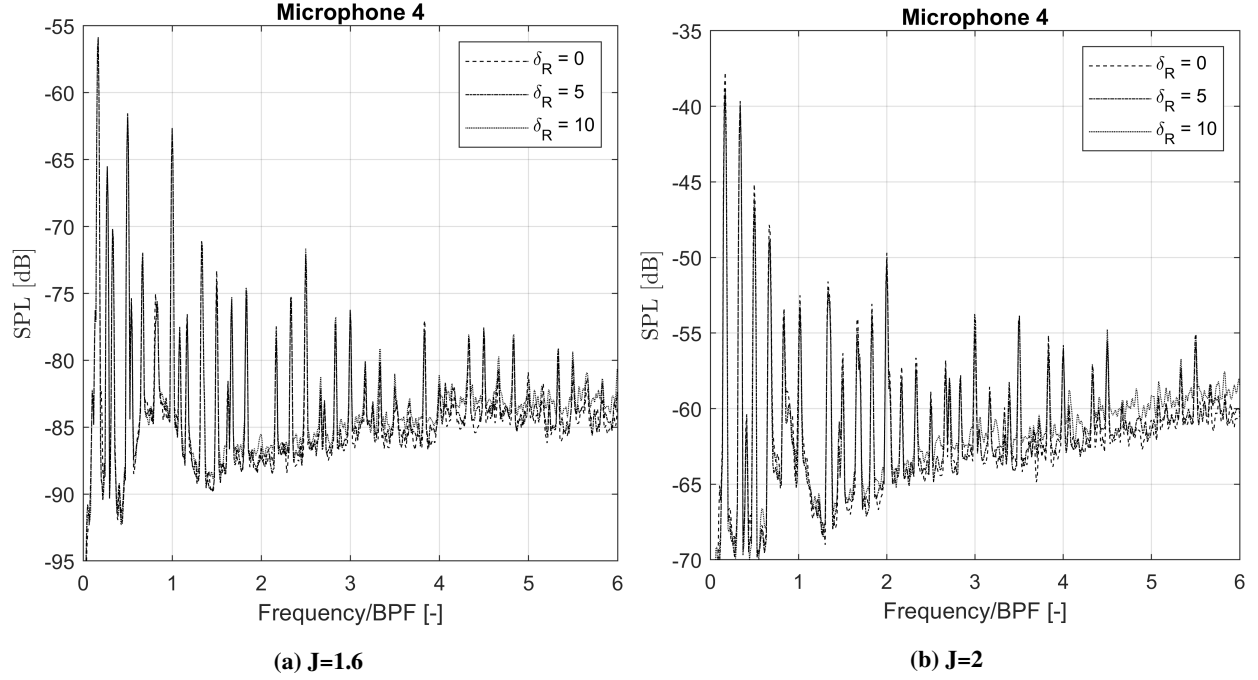


Fig. 20 Effect of rudder deflection on the normalized SPL at $Re = 2.3 \cdot 10^5$, $\alpha = 2$, $\beta = 5$

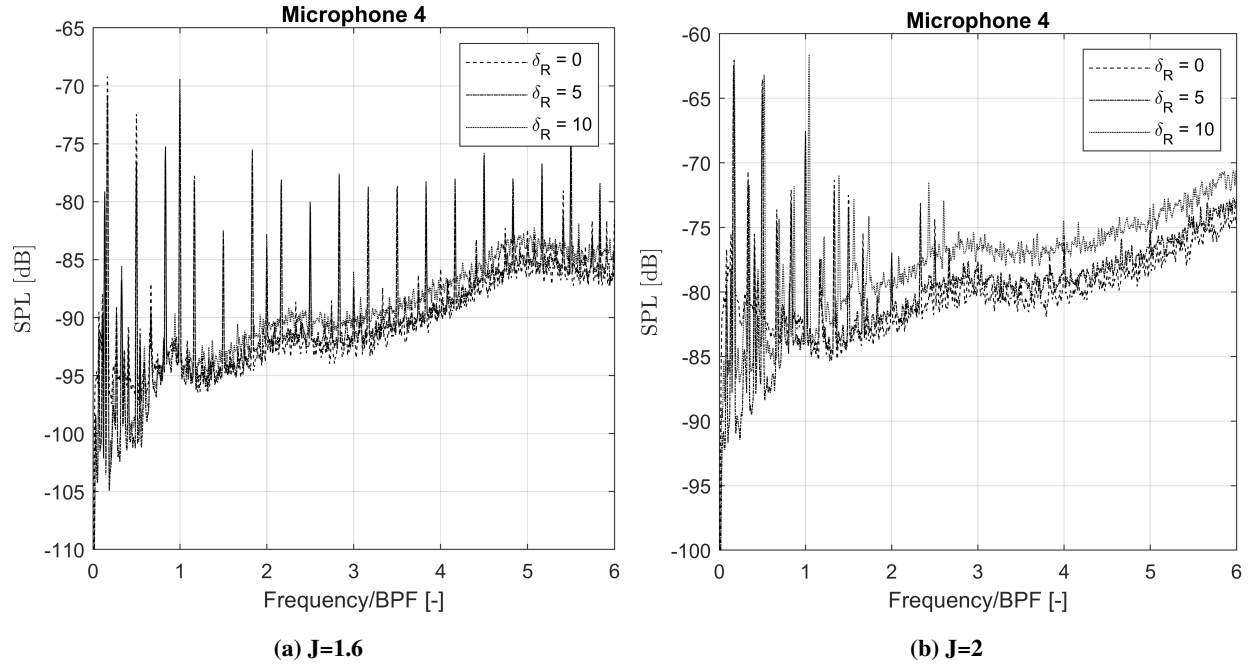


Fig. 21 Effect of rudder deflection on the normalized SPL at $Re = 4.6 \cdot 10^5$, $\alpha = 2$, $\beta = 5$

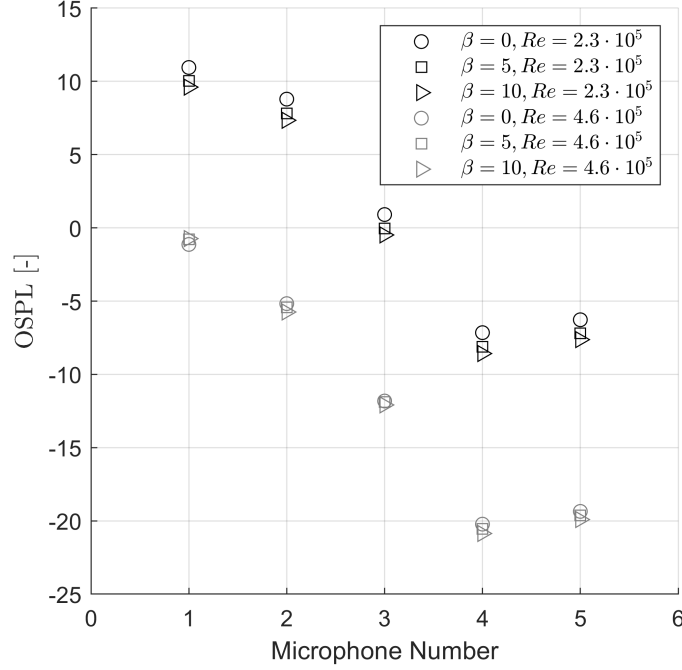


Fig. 22 Effect of sideslip variation on the normalized OSPL at $\alpha = 2, J = 1.8$

4.6. Limitations

As discussed previously, not all datapoints were used to determine the stability derivatives for the case with a Reynolds number of $2.3 \cdot 10^5$, due to non-linearity in the acquired data. Thus the obtained results are only valid for the full test envelope for $Re = 4.6 \cdot 10^5$. As aforementioned, the derivatives in this region visually match the derivatives in the calculated region. Due to this similarity and consistent occurrence, a systematic error in the acquisition of yaw and roll moment coefficients cannot be ruled out. When applying these results to the full-scale aircraft, it must be noted that the tested Reynolds numbers are not representative of the operations of the aircraft. As control and stability derivatives changed with Reynolds number, the controllability and stability of the full-scale aircraft may deviate significantly from the experimental data. Furthermore, the propeller performance varies significantly with Reynolds number, thus the measured performance will deviate from the performance of the full-scale aircraft as well.

With regards to the acoustic analysis, the microphone array being placed on the fuselage itself was a disadvantage, as the microphones would capture aerodynamic fluctuations along with acoustic fluctuations, and it is not possible to differentiate between them. Other disadvantages are that the measurement setup is not anechoic and the walls of the wind tunnel are not acoustically treated, due to which it is only possible to identify the tonal noise of the propeller. Therefore, it is not possible to differentiate between the background noise, the noise produced by the aircraft frame, propeller noise and noise caused by the support structures. Therefore, the acoustic analysis cannot be scaled to be applicable to a full-scale aircraft.

5. Conclusion and recommendations

From the collected data, it could be concluded that the aircraft is stable and controllable in one engine inoperative condition during cruise configuration. It was noticed that non-linear phenomena occur during low-speed operations at high angles of attack or low thrust settings. These effects are most likely caused by premature flow separation at the rudder for high angles of sideslip. Due to the predictable behaviour of moment coefficients in these regions, a systematic error in the measurement approach can neither be denied nor confirmed.

The quality of calculations of control and stability derivatives was assessed and found to be described by a linear model to a large extent. The effect of engine thrust on control derivatives was determined to be of the same order as a change in speed. To properly assess the cause and occurrence of non-linear effects at high angles of sideslip, more experiments should be performed between $\beta = 4$ deg and $\beta = 10$ deg. Results from these experiments can be used to determine if a systematic error was made in the acquisition of yawing and rolling moment coefficients. These effects, however, might not be representative for the real aircraft as the comparatively low Reynolds number of $2.3 \cdot 10^5$ will unlikely to be experienced in the aircraft's operation. In general, the controllability and stability of the full-scale aircraft may vary significantly from these results due to significantly different Reynolds numbers.

The acoustic performance was analysed at the different operating conditions and the tonal noise sources were identified. The effect of variation in the advance ratio on the noise generated at different Reynolds numbers was studied qualitatively as it was not possible to apply acoustic corrections to the current setup accurately. It was found that the tonal noise increased with increasing advance ratios, but the pressure signals decayed more rapidly at a higher Reynolds number. It was also observed that the rudder deflection angle has a negligible effect on the noise produced at low Reynolds numbers, whereas the sideslip angle has a minimal effect on the acoustic pressure at high Reynolds numbers. In conclusion, the acoustic results cannot be scaled to be representative of a full-scale aircraft due to the limitations of the wind tunnel setup.

References

- [1] Mulder, J., van Staveren, W., van der Vaart, J., de Weerd, E., de Visser, C., in 't Veld, A., and Mooij, E., “AE3202 Flight Dynamics Lecture Notes,” , 2013.
- [2] Sinnige, T., and Eitelberg, G., “Lab-Exercise Manual AE4115 Experimental Simulations,” , 2020.
- [3] Rae, W. H., and Pope, A., *Wind Tunnels*, Vol. 7, 1954. doi:10.1063/1.3061735.
- [4] Herriot, J. G., “Blockage corrections for three-dimensional-flow closed-throat wind tunnels, with consideration of the effect of compressibility,” *L*, , No. April, 1957, pp. 1–32.

A. Test Matrix

Engine 1 (starboard) is free-spinning during all tests. Engine 2 is the port engine

Start this polar at: 12:00								
Polar	DPN	δ_r [deg]	Motor direction	V_∞ [m/s]	Propeller <i>RPS</i> [Hz] (J [-])	α [deg]	β [deg]	Duration [s]
1	1	0	NO PROP	20	0.0 (0.0)	2.0	0.0	40
1	2	0	NO PROP	20	0.0 (0.0)	-1.0	2.0	40
1	3	0	NO PROP	20	0.0 (0.0)	5.0	2.0	40
1	4	0	NO PROP	20	0.0 (0.0)	-3.0	5.0	40
1	5	0	NO PROP	20	0.0 (0.0)	2.0	5.0	40
1	6	0	NO PROP	20	0.0 (0.0)	7.0	5.0	40
1	7	0	NO PROP	20	0.0 (0.0)	-1.0	8.0	40
1	8	0	NO PROP	20	0.0 (0.0)	5.0	8.0	40
1	9	0	NO PROP	20	0.0 (0.0)	2.0	10.0	40

Start this polar at: 12:11								
Polar	DPN	δ_r [deg]	Motor direction	V_∞ [m/s]	Propeller <i>RPS</i> [Hz] (J [-])	α [deg]	β [deg]	Duration [s]
2	10	0	NO PROP	40	0.0 (0.0)	2.0	0.0	40
2	11	0	NO PROP	40	0.0 (0.0)	-1.0	2.0	40
2	12	0	NO PROP	40	0.0 (0.0)	5.0	2.0	40
2	13	0	NO PROP	40	0.0 (0.0)	-3.0	5.0	40
2	14	0	NO PROP	40	0.0 (0.0)	2.0	5.0	40
2	15	0	NO PROP	40	0.0 (0.0)	7.0	5.0	40
2	16	0	NO PROP	40	0.0 (0.0)	-1.0	8.0	40
2	17	0	NO PROP	40	0.0 (0.0)	5.0	8.0	40
2	18	0	NO PROP	40	0.0 (0.0)	2.0	10.0	40

Start this polar at: 12:32								
Polar	DPN	δ_r [deg]	Motor direction	V_∞ [m/s]	Propeller <i>RPS</i> [Hz] (J [-])	α [deg]	β [deg]	Duration [s]
3	19	0	CCW	0	0.0 (0.0)	2.0	0.0	40
3	20	0	CCW	0	0.0 (0.0)	-1.0	2.0	40
3	21	0	CCW	0	0.0 (0.0)	5.0	2.0	40
3	22	0	CCW	0	0.0 (0.0)	-3.0	5.0	40
3	23	0	CCW	0	0.0 (0.0)	2.0	5.0	40
3	24	0	CCW	0	0.0 (0.0)	7.0	5.0	40
3	25	0	CCW	0	0.0 (0.0)	-1.0	8.0	40
3	26	0	CCW	0	0.0 (0.0)	5.0	8.0	40
3	27	0	CCW	0	0.0 (0.0)	2.0	10.0	40

Start this polar at: 12:38								
Polar	DPN	δ_r [deg]	Motor direction	V_∞ [m/s]	Propeller <i>RPS</i> [Hz] (J [-])	α [deg]	β [deg]	Duration [s]
4	28	0	CCW	0	0.0	0	0	40
4	29	0	CCW	20	61.5 (1.6)	2.0	5.0	40
4	30	0	CCW	20	58.6 (1.68)	-1.0	2.0	40
4	31	0	CCW	20	58.6 (1.68)	5.0	2.0	40
4	32	0	CCW	20	58.6 (1.68)	-1.0	8.0	40
4	33	0	CCW	20	58.6 (1.68)	5.0	8.0	40
4	34	0	CCW	20	54.7 (1.8)	2.0	0.0	40
4	35	0	CCW	20	54.7 (1.8)	-3.0	5.0	40
4	36	0	CCW	20	54.7 (1.8)	2.0	5.0	40
4	37	0	CCW	20	54.7 (1.8)	7.0	5.0	40
4	38	0	CCW	20	54.7 (1.8)	2.0	10.0	40
4	39	0	CCW	20	51.3 (1.92)	-1.0	2.0	40
4	40	0	CCW	20	51.3 (1.92)	5.0	2.0	40
4	41	0	CCW	20	51.3 (1.92)	-1.0	8.0	40
4	42	0	CCW	20	51.3 (1.92)	5.0	8.0	40
4	43	0	CCW	20	49.2 (2.0)	2.0	5.0	40

Start this polar at: 12:53								
Polar	DPN	δ_r [deg]	Motor direction	V_∞ [m/s]	Propeller <i>RPS</i> [Hz] (J [-])	α [deg]	β [deg]	Duration [s]
5	44	0	CCW	40	123.0 (1.6)	2.0	5.0	40
5	45	0	CCW	40	117.2 (1.68)	-1.0	2.0	40
5	46	0	CCW	40	117.2 (1.68)	5.0	2.0	40
5	47	0	CCW	40	117.2 (1.68)	-1.0	8.0	40
5	48	0	CCW	40	117.2 (1.68)	5.0	8.0	40
5	49	0	CCW	40	109.4 (1.8)	2.0	0.0	40
5	50	0	CCW	40	109.4 (1.8)	-3.0	5.0	40
5	51	0	CCW	40	109.4 (1.8)	2.0	5.0	40
5	52	0	CCW	40	109.4 (1.8)	7.0	5.0	40
5	53	0	CCW	40	109.4 (1.8)	2.0	10.0	40
5	54	0	CCW	40	102.5 (1.92)	-1.0	2.0	40
5	55	0	CCW	40	102.5 (1.92)	5.0	2.0	40
5	56	0	CCW	40	102.5 (1.92)	-1.0	8.0	40
5	57	0	CCW	40	102.5 (1.92)	5.0	8.0	40
5	58	0	CCW	40	98.4 (2.0)	2.0	5.0	40

Start this polar at: 13:18								
Polar	DPN	δ_r [deg]	Motor direction	V_∞ [m/s]	Propeller <i>RPS</i> [Hz] (J [-])	α [deg]	β [deg]	Duration [s]
6	59	5	CCW	0	0.0	0	0	40
6	60	5	CCW	20	61.5 (1.6)	2.0	5.0	40
6	61	5	CCW	20	58.6 (1.68)	-1.0	2.0	40
6	62	5	CCW	20	58.6 (1.68)	5.0	2.0	40
6	63	5	CCW	20	58.6 (1.68)	-1.0	8.0	40
6	64	5	CCW	20	58.6 (1.68)	5.0	8.0	40
6	65	5	CCW	20	54.7 (1.8)	2.0	0.0	40
6	66	5	CCW	20	54.7 (1.8)	-3.0	5.0	40
6	67	5	CCW	20	54.7 (1.8)	2.0	5.0	40
6	68	5	CCW	20	54.7 (1.8)	7.0	5.0	40
6	69	5	CCW	20	54.7 (1.8)	2.0	10.0	40
6	70	5	CCW	20	51.3 (1.92)	-1.0	2.0	40
6	71	5	CCW	20	51.3 (1.92)	5.0	2.0	40
6	72	5	CCW	20	51.3 (1.92)	-1.0	8.0	40
6	73	5	CCW	20	51.3 (1.92)	5.0	8.0	40
6	74	5	CCW	20	49.2 (2.0)	2.0	5.0	40

Start this polar at: 13:34								
Polar	DPN	δ_r [deg]	Motor direction	V_∞ [m/s]	Propeller <i>RPS</i> [Hz] (J [-])	α [deg]	β [deg]	Duration [s]
7	75	5	CCW	40	123.0 (1.6)	2.0	5.0	40
7	76	5	CCW	40	117.2 (1.68)	-1.0	2.0	40
7	77	5	CCW	40	117.2 (1.68)	5.0	2.0	40
7	78	5	CCW	40	117.2 (1.68)	-1.0	8.0	40
7	79	5	CCW	40	117.2 (1.68)	5.0	8.0	40
7	80	5	CCW	40	109.4 (1.8)	2.0	0.0	40
7	81	5	CCW	40	109.4 (1.8)	-3.0	5.0	40
7	82	5	CCW	40	109.4 (1.8)	2.0	5.0	40
7	83	5	CCW	40	109.4 (1.8)	7.0	5.0	40
7	84	5	CCW	40	109.4 (1.8)	2.0	10.0	40
7	85	5	CCW	40	102.5 (1.92)	-1.0	2.0	40
7	86	5	CCW	40	102.5 (1.92)	5.0	2.0	40
7	87	5	CCW	40	102.5 (1.92)	-1.0	8.0	40
7	88	5	CCW	40	102.5 (1.92)	5.0	8.0	40
7	89	5	CCW	40	98.4 (2.0)	2.0	5.0	40

Start this polar at: 13:59								
Polar	DPN	δ_r [deg]	Motor direction	V_∞ [m/s]	Propeller <i>RPS</i> [Hz] (J [-])	α [deg]	β [deg]	Duration [s]
8	90	10	CCW	0	0.0	0	0	40
8	91	10	CCW	20	61.5 (1.6)	2.0	5.0	40
8	92	10	CCW	20	58.6 (1.68)	-1.0	2.0	40
8	93	10	CCW	20	58.6 (1.68)	5.0	2.0	40
8	94	10	CCW	20	58.6 (1.68)	-1.0	8.0	40
8	95	10	CCW	20	58.6 (1.68)	5.0	8.0	40
8	96	10	CCW	20	54.7 (1.8)	2.0	0.0	40
8	97	10	CCW	20	54.7 (1.8)	-3.0	5.0	40
8	98	10	CCW	20	54.7 (1.8)	2.0	5.0	40
8	99	10	CCW	20	54.7 (1.8)	7.0	5.0	40
8	100	10	CCW	20	54.7 (1.8)	2.0	10.0	40
8	101	10	CCW	20	51.3 (1.92)	-1.0	2.0	40
8	102	10	CCW	20	51.3 (1.92)	5.0	2.0	40
8	103	10	CCW	20	51.3 (1.92)	-1.0	8.0	40
8	104	10	CCW	20	51.3 (1.92)	5.0	8.0	40
8	105	10	CCW	20	49.2 (2.0)	2.0	5.0	40

Start this polar at: 14:15								
Polar	DPN	δ_r [deg]	Motor direction	V_∞ [m/s]	Propeller <i>RPS</i> [Hz] (J [-])	α [deg]	β [deg]	Duration [s]
9	106	10	CCW	40	123.0 (1.6)	2.0	5.0	40
9	107	10	CCW	40	117.2 (1.68)	-1.0	2.0	40
9	108	10	CCW	40	117.2 (1.68)	5.0	2.0	40
9	109	10	CCW	40	117.2 (1.68)	-1.0	8.0	40
9	110	10	CCW	40	117.2 (1.68)	5.0	8.0	40
9	111	10	CCW	40	109.4 (1.8)	2.0	0.0	40
9	112	10	CCW	40	109.4 (1.8)	-3.0	5.0	40
9	113	10	CCW	40	109.4 (1.8)	2.0	5.0	40
9	114	10	CCW	40	109.4 (1.8)	7.0	5.0	40
9	115	10	CCW	40	109.4 (1.8)	2.0	10.0	40
9	116	10	CCW	40	102.5 (1.92)	-1.0	2.0	40
9	117	10	CCW	40	102.5 (1.92)	5.0	2.0	40
9	118	10	CCW	40	102.5 (1.92)	-1.0	8.0	40
9	119	10	CCW	40	102.5 (1.92)	5.0	8.0	40
9	120	10	CCW	40	98.4 (2.0)	2.0	5.0	40

Start this polar at: 12:11								
Polar	DPN	δ_r [deg]	Motor direction	V_∞ [m/s]	Propeller RPS [Hz] (J [-])	α [deg]	β [deg]	Duration [s]
2	121	10	NO PROP	40	0.0 (0.0)	2.0	0.0	40
2	122	10	NO PROP	40	0.0 (0.0)	-1.0	2.0	40
2	123	10	NO PROP	40	0.0 (0.0)	5.0	2.0	40
2	124	10	NO PROP	40	0.0 (0.0)	-3.0	5.0	40
2	125	10	NO PROP	40	0.0 (0.0)	2.0	5.0	40
2	126	10	NO PROP	40	0.0 (0.0)	7.0	5.0	40
2	127	10	NO PROP	40	0.0 (0.0)	-1.0	8.0	40
2	128	10	NO PROP	40	0.0 (0.0)	5.0	8.0	40
2	129	10	NO PROP	40	0.0 (0.0)	2.0	10.0	40

Start this polar at: 12:00								
Polar	DPN	δ_r [deg]	Motor direction	V_∞ [m/s]	Propeller RPS [Hz] (J [-])	α [deg]	β [deg]	Duration [s]
1	130	10	NO PROP	20	0.0 (0.0)	2.0	0.0	40
1	131	10	NO PROP	20	0.0 (0.0)	-1.0	2.0	40
1	132	10	NO PROP	20	0.0 (0.0)	5.0	2.0	40
1	133	10	NO PROP	20	0.0 (0.0)	-3.0	5.0	40
1	134	10	NO PROP	20	0.0 (0.0)	2.0	5.0	40
1	135	10	NO PROP	20	0.0 (0.0)	7.0	5.0	40
1	136	10	NO PROP	20	0.0 (0.0)	-1.0	8.0	40
1	137	10	NO PROP	20	0.0 (0.0)	5.0	8.0	40
1	138	10	NO PROP	20	0.0 (0.0)	2.0	10.0	40